ADVANCED ELECTRONIC MATERIALS
www.advelectronicmat.de

Tunable Optoelectronic Properties of WS_2 by Local Strain Engineering and Folding

Ahmed Raza Khan, Teng Lu, Wendi Ma, Yuerui Lu, and Yun Liu**

Local strain engineering is an exciting approach to tune optoelectronic properties of materials. Two-dimensional (2D) materials such as 2D transition metal dichalcogenides (TMDs) are particularly well-suited for this purpose due to their high flexibility and deformability. Local strain engineering in 2D TMDs is typically achieved via strained wrinkles. Wrinkles on thick TMD layers have been reported to show interesting photoluminescence enhancement due to bandgap modulation and funneling effect. However, the wrinkles in ultrathin TMDs are not investigated because they can easily fall down to form folds. Both wrinkles and folds are achieved simultaneously in 1–3L tungsten disulfide (WS_2) using a new fabrication technique. A layer-dependent reduction in surface potential is found for both folded layers and perfect packed layers due to the dominant interlayer screening effect. The strain produced from the wrinkles modulates the semiconductive junction properties significantly. Thermoionic modeling suggests that strained (1.6%) wrinkles can lower the Schottky barrier height (SBH) by 20%. Upon illumination, SBH reduces significantly due to photogenerated carriers. This is an important advance toward controlling the optoelectronic properties of 2D TMDs via strain engineering, with applications for electronics and optoelectronics devices.

1. Introduction

Tuning the optoelectronic properties of semiconductors is important for device fabrication and fundamental science.[1] Researchers have used various ways to tune the optoelectronic properties such as strain engineering,[2,3] doping,[4,5] defect engineering,[6] etc. Particularly, local strain engineering provides an effective and straightforward way to tune the optoelectronic properties of semiconductors such as bandgap, carrier mobility, binding energy of excitons,[2,3,7] which has therefore been broadly used to improve the device performance such as enhancement of solar cell efficiencies and generation of single photon emitters.[8–12]

Two dimensional (2D) atomic crystals such as 2D transition metal dichalcogenides (TMDCs) monolayers are an ideal platform to study strain engineering because they can withstand strain greater than 10%.[13] In addition, they can be folded or wrapped due to their high flexibility, making them promising candidates for stretchable and flexible electronics.[13–15] Using strain engineering of 2D TMDCs, researchers have successfully tuned optoelectronic properties.[16,17] For example, Desai et al. showed considerable photoluminescence (PL) enhancement on atomically thin tungsten diselenide (WSe_2) upon strain application.[18] Strain effect is used to increase the career mobility of ultrathin MoS_2, thus leading to an improvement in the performance of MoS_2-based field effect transistor.[19]

Local strain engineered in 2D TMDs is typically achieved through stretching of a flexible substrate.[20] This method involves the exfoliation of 2D material on a prestretched flexible substrate followed by the formation of strained wrinkles after the release of the stretched substrate.[21] The wrinkles in ultrathin TMDs easily fall down to form folds due to their low bending rigidity.[20] Therefore, wrinkles formation in thick TMDs (layer ≥ 3) is only reported.[3,20] The excitons in thick wrinkles are reported to funnel toward the middle of the wrinkle's region; therefore, the wrinkles can change the local confinement potential of excitons.[3] Wrinkles are also reported to show exciting bandgap modification in atomically thin MoS_2.[3] PL measurements on 3–5L wrinkles indicate that bandgap energy decreases significantly as uniaxial strain increases. The experimental measurements showed ≈45.2 meV per % strain reduction in indirect bandgap whereas ≈32 meV per % strain reduction is found in direct bandgap (k–k' valley transition). This significant bandgap shift is also proved for wrinkles using tight-binding model.[3] The change of optical and electrical properties in strain induced wrinkles has also been observed with other 2D materials as well.[22–24] Several studies have reported the strain dependent bandgap reduction ≈27–46 meV per strain%[7,25,26] in monolayer tungsten disulfide (WS_2).

A. R. Khan, W. Ma, Prof. Y. Lu
Research School of Electrical, Energy and Materials Engineering
College of Engineering and Computer Science
Australian National University
ACT 2601, Canberra, Australia
E-mail: yuerui.lu@anu.edu.au; yun.liu@anu.edu.au
A. R. Khan
Department of Industrial and Manufacturing Engineering
University of Engineering and Technology (Rachna College)
Lahore 54700, Pakistan
Dr. T. Lu, Prof. Y. Liu
Research School of Chemistry
Australian National University
ACT 2601, Canberra, Australia

The ORCID identification number(s) for the author(s) of this article can be found under https://doi.org/10.1002/aelm.201901381.

DOI: 10.1002/aelm.201901381

Here, we have developed a new method, mechanical buckling of flexible substrate, to create both wrinkles and folds simultaneously in 1–3L WS_2 by successfully controlling the strain. The Kelvin probe force microscope (KPFM) and conductive atomic force microscope (CAFM) are used for surface potential mapping and current mapping, respectively. A layer dependent reduction in surface potential is found due to the dominant interlayer screening effect irrespective of the layers' orientation. The current mappings demonstrate strain tuning of semiconductive junction properties of strain-induced wrinkles. This behavior is explained using Thermionic model which suggests 1.6% strain on wrinkle nanostructures reduce 20% of Schottky barrier height (SBH). Photoconductive atomic force microscope (PCAFM investigation reveals that the SBH can be further lowered due to photo-enhanced current. Our results demonstrate an important advance toward controlling the properties of atomically thin WS_2 via strain induced wrinkling and folding. Moreover, these techniques could be applied to other 2D materials[27–36] and heterostructures[37–40] for applications in quantum optics, nanophotonics, and optoelectronics.

2. Results and Discussions

We employed mechanical buckling of the flexible substrate to achieve both wrinkles and folds simultaneously in 1–3L WS_2. The details of the fabrication method are shown in **Figure 1**a. i) The WS_2 flakes are exfoliated on a prebuckled gel polymer film. ii) After exfoliation, the buckled Gel film is released causing compressive forces on the exfoliated WS_2 flakes. The compressive forces generate big and tiny wrinkles. iii) The big wrinkles are formed in the direction perpendicular to the compressive forces (*x*-direction) and they fall down to form folds, iv) whereas the tiny wrinkles are generated in the direction parallel to the compressive forces (*y*-direction). The tiny wrinkles maintain their wrinkles like curvature which is explained later. In the text, the terms of big wrinkles and folds are used interchangeable. Without the specific notation, winkles present tiny wrinkles. A 3D schematic of the folds and wrinkles' formation after mechanical buckling is shown in Figure 1b. The buckled WS_2 sample is transferred onto a Si/SiO_2/gold electrode substrate.[41,42] Phase shifting interferometry (PSI)[28,30,43–45] is employed to identify the layer number of the WS_2 flakes (Figure S1, Supporting Information).

It is unambiguous that big wrinkles are formed perpendicular to the compressive forces (antiparallel red arrows) as depicted in optical image of buckled WS_2 (Figure 1c). Intriguingly, along with big wrinkles, some tiny wrinkles are also detected and their alignment is almost perpendicular to the big wrinkles as revealed by AFM topography (Figure 1d). The width of the tiny wrinkles (100–190 nm) is much smaller than that of the width of the big wrinkles, which is the possible reason why there is no trace of tiny wrinkles under the optical microscope. The inset plot (red rectangle) of Figure 1d gives detailed height profiles of both big

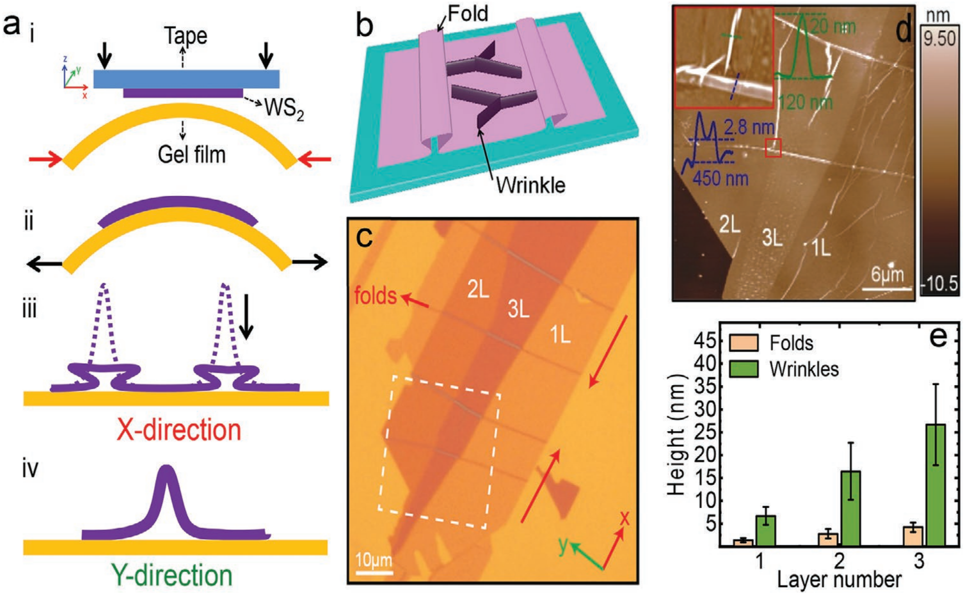

Figure 1. Creation of wrinkles and folds in 1–3L WS_2. a) Schematic diagram of the fabrication process for wrinkles and folds formation in atomically thin WS_2. (i) An elastomeric substrate (Gel film) is buckled prior depositing WS_2 flakes using a tape. (ii) The buckled substrate is released causing compressive forces which create big and tiny wrinkles perpendicular and parallel, respectively, to the direction of forces (*X*-direction). (iii) Big wrinkles fall down to form folds (*X*-direction view) (iv) whereas tiny wrinkles retain their shape (*Y*-direction view). b) A 3D image of strained sample showing wrinkles and folds, different colors for the wrinkles and the folds are used for clear visibility. c) Optical microscopic image of 1–3L strained WS_2 sample fabricated by the method described above; folds are created perpendicular to the direction of the compressive forces, two antiparallel arrows (red color) indicate the direction of the compressive force. d) AFM topography image of the region marked by the white dashed rectangle in (c) whereas inset image is the zoom-in view of the small red rectangle. Inset image shows AFM measurement of the wrinkle (20 nm height and 120 nm width) and fold (2.8 nm height and 450 nm width) in green and blue colors, respectively. e) The layer dependence of wrinkles and height differences for folds measured on 1L, 2L, and 3L. The histogram shows the AFM height measurements, with variation in measurements indicated by the error bars. The orange and green rectangles indicate the height measurements for folds and wrinkles respectively.

and tiny wrinkles which indicate that the height of big wrinkles is much smaller than the tiny wrinkles. Moreover, height profile of tiny wrinkles presents a sharp peak-shaped cross-section in contrary to big wrinkles which present an almost rectangular shaped cross-section. According to this profile, we assume that big wrinkles form folds whereas tiny wrinkles are the wrinkles maintaining their curvature. Figure 1e plots the height difference between the big/tiny wrinkle and corresponded flat regions. For the big wrinkles, the height differences measured on 1L, 2L, and 3L samples are 1.4 ± 0.5, 2.8 ± 0.5, and 4.2 ± 1 nm, respectively. These values match the height of 2L, 4L, and 6L samples very well as the thickness of single layer is evaluated around 0.7 nm, which agrees well with the reported value.[46] Therefore, the big wrinkles can be regarded as the bifolded samples, e.g., the big wrinkle on the 1L sample can be considered as bifolded single layer (1L + 1L + 1L) samples and its height is in good consistency with the pristine 3L sample. In a previous work on MoS_2,[3] the appearance of the fold regions is possibly ascribed to the collapsing of the large wrinkles caused by the buckling-induced delamination. Such wrinkle to fold transition is also observed on monolayers of graphene and TMDC by researchers in the past.[20,47–49] It is worthy to note that the tiny wrinkles appear in the center of the nanoflakes and therefore, their height values present large deviations. However, their deformation is relatively small and they maintain their wrinkles' like curvature. The maximum uniaxial strain ε is accumulated on top of the winkles and can be estimated as[3]

$$\varepsilon \sim \pi^2 h\delta/(1-\nu^2)\lambda^2 \tag{1}$$

where ν is the Poisson's ratio ($\nu = 0.22$ for WS_2[50]), h is the thickness of the flake, and δ and λ are the height and width of the wrinkle, which were measured using AFM. The relationship shows that the height of the wrinkles increases with the strain applied. For the wrinkles' profile on 2L WS_2 given in Figure 1d (green color), strain ε can be estimated as 2% where $h = 1.4$ nm, $\delta = 20$ nm, $\lambda = 120$ nm.

Wrinkling requires a minimum value of strain to initiate the wrinkles formation. As the strain increases, the height of the wrinkles increases. After a critical strain level (ε_f), wrinkles cannot maintain their curvature and collapse forming folds (Figure S2c, Supporting Information). Critical strain level is dependent on layer thickness and elastic modulus of ultrathin WS_2 film (see Section S3 of the Supporting Information for more details). As layer number increases, ε_f increases and fold formation in higher layer number decreases. Therefore, wrinkle to fold transition is dominant in small layer number (1L > 2L > 3L) due to their low critical strain (ε_f). Moreover, it can also be found that wrinkles' average height increases as layer number increases (3L > 2L > 1L), which can be attributed to increasing critical strain level (ε_f) in higher layer number showing more capability to maintain wrinkles' curvature (Figure 1e). Additionally, the width of the folds also showed an increase as layer number increases, which ranges 180–400, 250–450, and 350–500 nm for 1L, 2L, and 3L, respectively.

2.1. Surface Potential Measurements

With intentional manufacturing, we have obtained different local features (flat, fold, and wrinkles) in 1–3L WS_2. As varying the local stacking and strain states of the WS_2 samples, the electronic structures are expected to be tuned. KPFM is a useful tool to map the surface potential at the nanometer scale. In KPFM, an AC bias is applied to a conductive tip to produce an electrical force, which is minimized when contact potential difference or surface potential between tip and sample is compensated by an applied DC bias. In principle, the contact potential difference (V_{CPD}) is originated from the different work functions between the tip and the sample, which can be expressed as follows[51,52]

$$V_{CPD} = \frac{\Phi_{tip-}\ \Phi_{sample}}{-e} \tag{2}$$

where Φ_{tip} and Φ_{sample} are work functions of the tip and the sample and e is the electronic charge. However, in reality, many factors such as trapped charges, tip damage, and permanent dipoles between the sample and the tip will impact the results. Therefore, KPFM usually gives an accurate measurement of the potential difference rather than the absolute value. The surface potential mapping is carried out for the flat, folded, and wrinkled regions of 1–3L WS_2. The typical morphology and surface potential images are presented in **Figure 2**a–d. The potential measured on different layers presents evident contrast. Combining the morphology mapping, in the 1L, 2L, and 3L samples, the surface potential in fold regions is unambiguously lower than the flat regions for the similar layer number. However, no clear features are obtained for wrinkles in surface potential mapping, which can be ascribed to the small size (width ≈100–190 nm) of wrinkles making it to be difficult to be resolved. In order to conduct quantitative analysis on folded regions, the surface potential values are calculated by fitting the histograms collected from different domains (Figure S3, Supporting Information). The offsets (Figure 2b,d) exhibit a small divergence, therefore, the surface potential of flat 3L sample is considered as the reference to make the measured values comparable. As shown in Figure 2e,f, the surface potential of flat and folded regions decreases linearly with an increase in layer number. The differences between each layer are ≈23 and 9.5 mV for flat and folded regions, respectively. Taking the KPFM set-up into the consideration, work function increases as layer number increases, which is consistent with the previous studies on layer dependent work function of flat MoS_2.[53,54] The layer-dependent work function can be explained by the dominant interlayer screening effect, which is also reported for other materials also such as graphene and MoS_2.[55–57] Geometrically, the layer number of folded regions is comparable with the pristine 3L, 6L, and 9L samples while the twisted stacking will result in the change of the interlayer coupling in comparison with the perfect packing samples. Intriguingly, no distinct difference is obtained between the surface potential of bifolded 1L and flat 3L samples, indicating the interlayer screening effect is dominant in WS_2 folds irrespective of the layer orientation.

2.2. Dark Carrier Transport

The charge transport behavior is important characteristic for the semi conductive device performance. This section will focus on charge transportation for flat, folded, and winkled

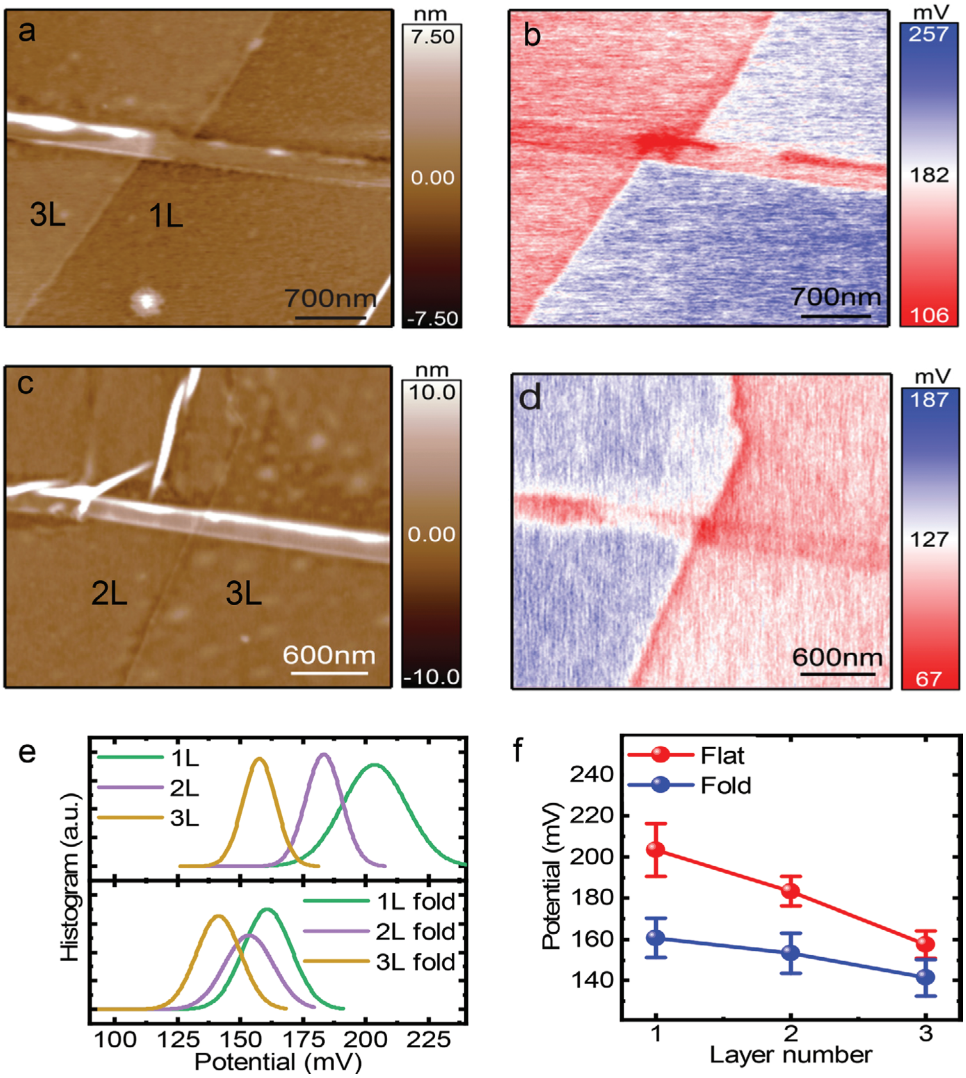

Figure 2. Layer-dependent surface potential of folds in 1–3L WS_2. a) AFM topography image, showing the flat, folded, and wrinkled regions on 1L and 3L. b) Surface potential mapping of (a). c) AFM topography image, showing the flat, folded, and wrinkled regions on 2L and 3L. d) Surface potential image of the region shown in (c). e) Surface potential histogram of 1–3L flat WS_2 (upper panel) and 1–3L fold WS_2 (lower panel). f) Surface potential of 1–3L flat WS_2 (red) and 1–3L fold WS_2 (blue), with variation in the readings is indicated by the error bars.

regions. A schematic of the set-up for the conductive and photoconductive atomic force microscopy (CAFM and PCAFM) is shown in **Figure 3**a. The CAFM tip acts as the top electrode and gold is the bottom electrode. In dark condition (no light), the current mappings of AFM topographic image (red rectangle) are done under 4 and 10 V bias (Figure 3b,c). No evident current is detected overall under 4 V except some traces at the wrinkled regions. With increasing the bias to 10 V, the wrinkles exhibit significant enhancement of electrical current flow and current reaches around 400 pA. The local *I*–*V* curves on different regions are measured to further investigate the electronic properties as shown in Figure 3d. At the low bias, the currents measured at flat, folded, and wrinkled regions exhibit nearly insulating behavior while the diode-like characteristics are obtained by gradually increasing the bias. SBH, Φ_b, measured at wrinkled regions is lower than those measured at flat and folded regions which will be explained later. The distance to the bottom gold electrode is similar (≈20 µm) for three regions. Therefore, we can assume the obtained *I*–*V* behaviors are mainly determined by the metal tip–semiconductor contact resistance. Due to the difference between the tip work function and electron affinity of WS_2, Schottky barrier is formed at the interface. Figure 3e illustrates the equilibrium case of Schottky barrier between CAFM tip and WS_2 (flat and wrinkle). It is evident SBH represented by Φ_b ($\Phi_b = \Phi_{tip} - \chi$, where χ is the WS_2 electron affinity), is the determinant factor for the current flow.[58,59] Li et al.[56] performed a CAFM study on ultrathin MoS_2 using a conductive tip and successfully explained the characteristics of the resulting junction in the forward bias regime using thermionic emission model. Therefore, the current under forward bias can be described by the thermionic emission model over the Schottky barrier as under[60]

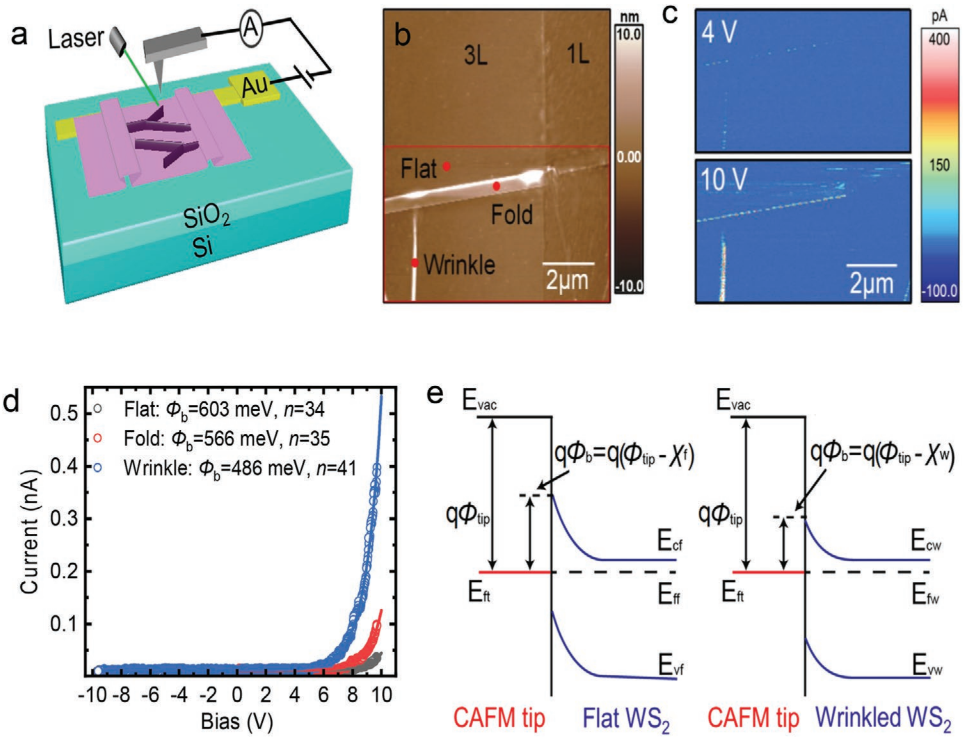

Figure 3. Current mapping of wrinkles in atomically thin WS_2 by conductive AFM imaging. a) A schematic of conductive AFM configuration for carrier transport measurements. Strained sample is transferred onto a gold electrode and the voltage is applied on the sample under forward bias. b) AFM topography image, showing the flat, folded, and wrinkled regions. c) Current mapping of the region marked by red rectangle in (b) under bias voltages of 4 and 10 V. d) A current–voltage (*I–V*) curve for flat, fold, and wrinkle indicated by red dots in (b) under (−10 to +10 V) bias voltage, Schottky barrier height (Φ_b) for flat = 603 meV, fold = 566 meV, and wrinkle = 486 meV is calculated using thermionic model. The corresponding strain for the wrinkle is calculated to be 1.6%. e) Energy band diagram for CAFM tip–WS_2 (flat) and CAFM tip–WS_2 (wrinkled) junction. Φ_{tip} is the CAFM tip work function, E_{vac} is the reference vacuum level, q is the charge, Φ_b is the barrier height, χ_f and χ_w are electron affinity for flat and wrinkle WS_2, respectively, E_{ft}, E_{ff}, and E_{fw} are the Fermi level of the tip, flat, and wrinkle WS_2, respectively. E_{vf} and E_{cf} are valence and conduction band levels of flat WS_2 whereas E_{vw} and E_{cw} are valence and conduction band levels of wrinkle WS_2.

$$I = A_{tip} A^* T^2 e^{-\frac{q\phi_B}{kT}} e^{\frac{q(V-IR)}{nkt}} \tag{3}$$

where A_{tip} is the tip–sample contact area, $A^* = 4\pi qk^2 m_{eff}/h^3$ is the Richardson constant with effect mass for electrons $\approx 0.3m_e$ for WS_2,[61] h is the Planck constant, T is the temperature which equals ≈300 K, q is the elementary charge and Φ_B is the SBH, k is Boltzmann constant, R is the resistance in the circuit, and n is the ideality factor. Since the current value is quite small (<500 pA), the voltage drops across the Schottky barrier (V-IR) is almost equal to the applied bias. The fitting parameters for the three curves are displayed in Figure 3d. The large ideality factor, n = 34, 35, and 41 for flat, fold, and wrinkle suggests the thermionic emission model requires careful consideration while Φ_b fitted for the flat sample is around 603 meV, which is close to the recently reported Φ_b = 590 meV between the Pt-coated tip and WS_2 nanoflake.[62] The fitting results suggest different *I–V* characteristics collected from flat, folded, and wrinkled regions are originated from the different SBH formation at the metal–semiconductor interface. A large reduction of Φ_b (≈486 meV) is obtained for the wrinkled WS_2 junction as compared to the flat WS_2 junction whereas the strain is calculated to be 1.6% on the wrinkle using Equation (1). Previously, researchers have reported strain-induced bandgap reduction in ultrathin WS_2,[7,63] which can be attributed to lowering of SBH in wrinkled WS_2. The bandgap generally decreases with increasing the thickness in 2D TMDs semiconductors.[64,65] Therefore, we find a reduction in SBH of tip–WS_2 (fold) junction, which is in good agreement with a previous study showing SBH reduction with increasing the thickness of MoS_2 in MoS_2–metal contact.[66] However, it is still worthy to note that the folding of 2D materials could change the stacking orders among the layers, thereby tuning interlayer coupling and band structures.[67]

2.3. Photocarrier Transport

In the previous sections, we successfully demonstrated strain engineering and folding as powerful tools to tune the electronic properties. Strain engineering and folding are also expected to tune optoelectronic properties. In this context, the current mappings of the topographic image (red rectangle in Figure 3b) are carried out under dark (no light) and light condition for direct comparison. It is evident that current flow under illumination is enhanced for all the regions (flat, fold, and wrinkle). However, wrinkled regions present the strongest contrast compared with other two regions.

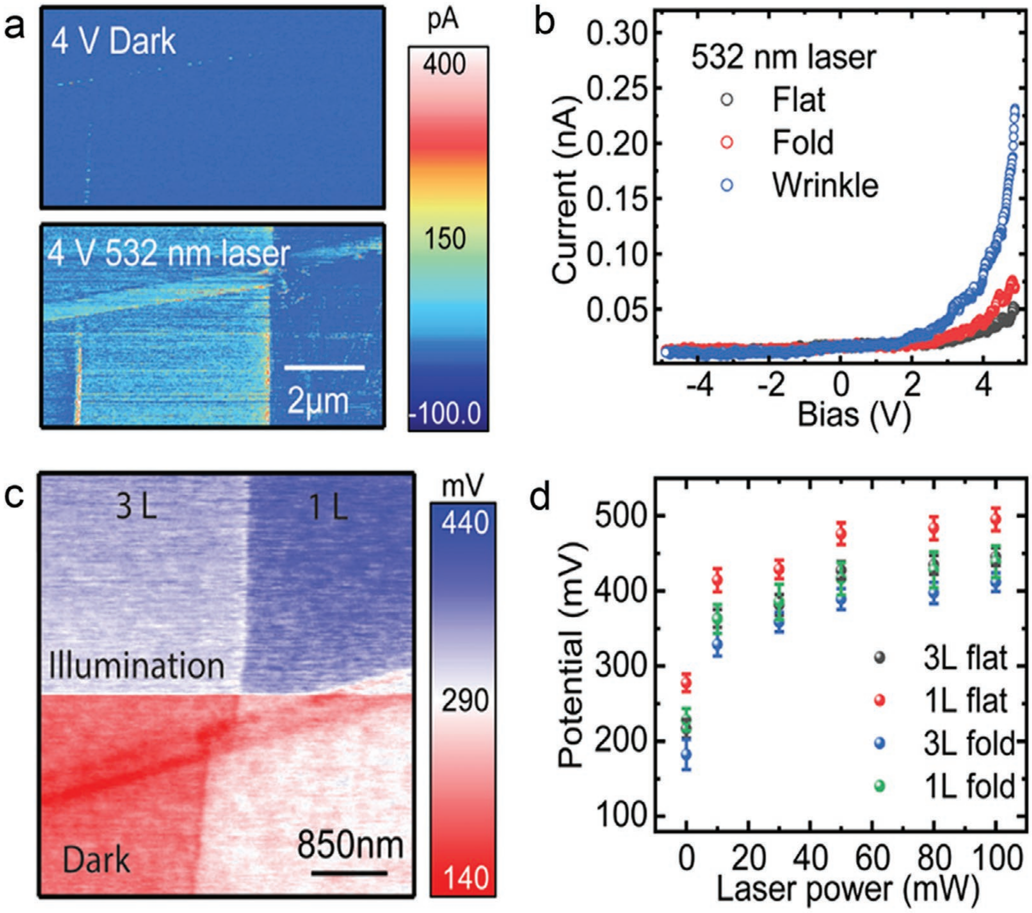

Figure 4. Differentiation of wrinkled and folded nanostructures by photoconductive AFM. a) Current mapping (of the region marked by red rectangle in Figure 3c) under dark (no light) and light (60 mW) at forward biased voltage of 4 V. b) Current–voltage (*I–V*) curve showing photocurrent response for flat, fold, and wrinkle under excitation from a 532 nm laser with 60 mW power density. c) Surface potential mapping of 1L and 3L under dark (no light) and light (60 mW). d) Laser power dependent surface potential (mV) response of 1 and 3L flat and fold under excitation from a 532 nm laser with 60 mW power density. Error bars indicate the variation in measurements.

I–V junction characteristics of flat, folded, and wrinkled region under illumination are presented to further explore this behavior (**Figure** 4b). Here, *I–V* curves present rectifying characteristics with 5 V forward bias under illumination whereas no obvious current responses were obtained for three regions using the same applied voltage under the dark condition. Furthermore, a small photocurrent is detectable under the zero voltage bias, which might be arisen from the tiny photoresponse compared with the instrumental current threshold (≈10 pA) or small work function difference between the top and bottom electrodes (Pt/Ir tip and Au). Enhancement of the electrical current under illumination might have a close relationship with the photogenerated carriers. As the *I–V* curves still exhibit diode-like features, it can be proposed that the current flowing in the circuit is mainly decided by the metal/semiconductor contact resistance. Through adopting the thermionic model, either increasing the temperature or decreasing the SBH can intensify the current. Both current mapping and time-resolved photoresponse under the repeated on–off light irradiation indicate the hysteresis, which is normally due to the thermal effect, is not obvious in flat WS_2 samples (Figures S5 and S6, Supporting Information). To further investigate the impacts of photogenerated carriers on SBH, the surface potential under the light irradiation is shown in Figure 4c. It is obvious that the surface potentials on both flat and folded regions exhibit an abrupt increase when the incident laser is on. Figure 4d shows the surface potential variation as a function of the incident laser power measured in the same region. The detailed surface potential images can be found in Figure S7 of the Supporting Information. For both the flat and folded regions, the biggest variation occurs when the laser is switched on, which indicates that the surface potential change mainly originates from the photoexcitation rather than the thermal-excitation. According to the KPFM set-up, the increase of surface potential is a consequence of accumulated positive charges on the surface or the appearance of upward dipole moment.[68] Both effects can bend the band structure of WS_2 samples, lowering the SBH. Therefore, the photo-enhanced current is attributed to lowering the SBH by the photogenerated current.

3. Conclusion

In summary, we have successfully demonstrated the fabrication of both fold and wrinkle nanostructures simultaneously in 1–3L WS_2 by controlling strain. It is found that the interlayer screening effect is the dominant factor in layer dependent surface potential measurements. Therefore, we find layer dependent surface potential reduction for both perfect pack and twisted layers of ultrathin WS_2. The current mappings demonstrate strain tuning of semi conductive junction properties of strain induced wrinkles. This behavior is explained using Thermoionic model, which suggests 20% reduction in Schottky barrier height through 1.6% strain on wrinkle. PCAFM investigation reveals further lowering of SBH due to photogenerated carriers. Our technique offers a route to local strain engineering in ultrathin materials, opening up many applications in diverse fields such as electronics, quantum optics, optoelectronics, and surface science.

4. Experimental Section

Sample Fabrication: WS_2 flakes were exfoliated onto buckled elastomeric substrate (Gel-Film WF 6.0mil × 4 films) using scotch tape. Subsequently, the Gel film was suddenly released, generating well-aligned folds and wrinkles in WS_2 layers due to the application of compressive forces because of the sudden release. Sudden release of the prestress films was found to give a higher yield of folds and wrinkles in WS_2 layers. Strained WS_2 sample was transferred onto $Au/SiO_2/Si$ electrode substrates followed by adhesively bonding an iron pad using copper tape to connect with AFM for further characterizations. AFM, PSI, and Raman spectroscopy were used to detect the layer numbers.

Surface Potential Measurements: Surface potential measurements were done using AFM (Asylum Research, Cypheras) after carrying out the procedures described in the Sample Fabrication section. Pt/Ir coated Si tip (nanosensor PPP-EFM) with a calibrated spring constant ≈1.9 N m^{-1} and radius of 28 ± 10 nm was used to conduct KFPM measurement. The tip was scan above ≈10 nm higher than the surface in the noncontact mode with a drive frequency of 70 kHz and 1 V AC voltage. The SP mapping images by KPFM (scan size: 3 µm × 3 µm) were obtained, where the temperature was maintained at room temperature.

Dark and Photocurrent Scanning: The Current and Photocurrent measurements were conducted on AFM in ambient conditions using Pt. tip, as illustrated in Figure 3a. Contact mode was used during the current scanning AFM. Topographic and Current images were obtained simultaneously so that topography and local currents can be compared directly. Most images were 512 × 512 pixels. For photocurrent measurements, the illumination source was 532 nm laser. During certain measurements, neutral density filters were used to modulate the laser intensity. AFM images were analyzed and plotted using the Gwyddion software package.

Supporting Information

Supporting Information is available from the Wiley Online Library or from the author.

Acknowledgements

A.R.K. and T.L. contributed equally to this work. The authors would like to acknowledge the financial support from Australian National University, Australia and Faculty Development Program funding under University of Engineering and Technology (UET) Lahore, Pakistan and Rachna College of Engineering and Technology (RCET), Gujranwala, Pakistan. Y.L. and Y. L. conceived and supervised the project; A.R.K. and W.M. prepared the samples; T.L. conducted the surface potential and current measurements; A. R. K. did the PSI and PL measurements. A.R.K. and T.L. cowrote the paper; all authors discussed the results and commented on the manuscript.

Conflict of Interest

The authors declare no conflict of interest.

Keywords

2D materials, charge transfer, strain engineering, WS_2

Received: December 11, 2019
Revised: February 10, 2020
Published online:

---

[1] E. J. G. Santos, E. Kaxiras, *ACS Nano* **2013**, *7*, 10741.
[2] J. Quereda, J. J. Palacios, N. Agräit, A. Castellanos-Gomez, G. Rubio-Bollinger, *2D Mater.* **2017**, *4*, 021006.
[3] A. Castellanos-Gomez, R. Roldán, E. Cappelluti, M. Buscema, F. Guinea, H. S. J. Van Der Zant, G. A. Steele, *Nano Lett.* **2013**, *23*, 534.
[4] Y. Du, H. Liu, A. T. Neal, M. Si, P. D. Ye, *IEEE Electron Device Lett.* **2013**, *34*, 1328.
[5] M. Fontana, T. Deppe, A. K. Boyd, M. Rinzan, A. Y. Liu, M. Paranjape, P. Barbara, *Sci. Rep.* **2013**, *3*, 1634.
[6] J. Pei, X. Gai, J. Yang, X. Wang, Z. Yu, D. Y. Choi, B. Luther-Davies, Y. Lu, *Nat. Commun.* **2016**, *7*, 10450.
[7] L. Wang, A. Kutana, B. I. Yakobson, *Ann. Phys.* **2014**, *526*, L7.
[8] J. Kern, I. Niehues, P. Tonndorf, R. Schmidt, D. Wigger, R. Schneider, T. Stiehm, S. Michaelis de Vasconcellos, D. E. Reiter, T. Kuhn, R. Bratschitsch, *Adv. Mater.* **2016**, *28*, 7101.
[9] C. Palacios-Berraquero, D. M. Kara, A. R. P. Montblanch, M. Barbone, P. Latawiec, D. Yoon, A. K. Ott, M. Loncar, A. C. Ferrari, M. Atatüre, *Nat. Commun.* **2017**, *8*, 15093.
[10] A. Branny, S. Kumar, R. Proux, B. D. Gerardot, *Nat. Commun.* **2017**, *8*, 15053.
[11] J. Feng, X. Qian, C. W. Huang, J. Li, *Nat. Photonics* **2012**, *6*, 866.
[12] H. Li, A. W. Contryman, X. Qian, S. M. Ardakani, Y. Gong, X. Wang, J. M. Weisse, C. H. Lee, J. Zhao, P. M. Ajayan, J. Li, H. C. Manoharan, X. Zheng, *Nat. Commun.* **2015**, *6*, 7381.
[13] L. Mennel, M. M. Furchi, S. Wachter, M. Paur, D. K. Polyushkin, T. Mueller, *Nat. Commun.* **2018**, *9*, 516.
[14] S. Bertolazzi, J. Brivio, A. Kis, *ACS Nano* **2011**, *5*, 9703.
[15] D. Akinwande, N. Petrone, J. Hone, *Nat. Commun.* **2014**, *5*, 5678.
[16] K. P. Dhakal, S. Roy, H. Jang, X. Chen, W. S. Yun, H. Kim, J. Lee, J. Kim, J. H. Ahn, *Chem. Mater.* **2017**, *29*, 5124.
[17] T. Shen, A. V. Penumatcha, J. Appenzeller, *ACS Nano* **2016**, *10*, 4712.
[18] S. B. Desai, G. Seol, J. S. Kang, H. Fang, C. Battaglia, R. Kapadia, J. W. Ager, J. Guo, A. Javey, *Nano Lett.* **2014**, *14*, 4592.
[19] Y. Chai, S. Su, D. Yan, M. Ozkan, R. Lake, C. S. Ozkan, *Sci. Rep.* **2017**, *7*, 41593.
[20] A. Castellanos-Gomez, H. S. J. van der Zant, G. A. Steele, *Nano Res.* **2014**, *7*, 572.
[21] A. Castellanos-Gomez, R. Roldán, E. Cappelluti, M. Buscema, F. Guinea, H. S. J. Van Der Zant, G. A. Steele, *Nano Lett.* **2013**, *13*, 5361.

[22] H. Hattab, A. T. N'Diaye, D. Wall, C. Klein, G. Jnawali, J. Coraux, C. Busse, R. Van Gastel, B. Poelsema, T. Michely, F. J. Meyer Zu Heringdorf, M. Horn-Von Hoegen, *Nano Lett.* **2012**, *12*, 678.
[23] L. Meng, Y. Su, D. Geng, G. Yu, Y. Liu, R. F. Dou, J. C. Nie, L. He, *Appl. Phys. Lett.* **2013**, *103*, 251610.
[24] J. Quereda, P. San-Jose, V. Parente, L. Vaquero-Garzon, A. J. Molina-Mendoza, N. Agraït, G. Rubio-Bollinger, F. Guinea, R. Roldán, A. Castellanos-Gomez, *Nano Lett.* **2016**, *16*, 2931.
[25] X. He, H. Li, Z. Zhu, Z. Dai, Y. Yang, P. Yang, Q. Zhang, P. Li, U. Schwingenschlogl, X. Zhang, *Appl. Phys. Lett.* **2016**, *109*, 173105.
[26] Q. Zhang, Z. Chang, G. Xu, Z. Wang, Y. Zhang, Z. Q. Xu, S. Chen, Q. Bao, J. Z. Liu, Y. W. Mai, W. Duan, M. S. Fuhrer, C. Zheng, *Adv. Funct. Mater.* **2016**, *26*, 8707.
[27] G. P. Neupane, W. Ma, T. Yildirim, Y. Tang, L. Zhang, Y. Lu, *Nano Mater. Sci.* **2019**, *1*, 246.
[28] J. Pei, J. Yang, Y. Lu, *IEEE J. Sel. Top. Quantum Electron.* **2017**, *23*, 206.
[29] K. Cho, J. Yang, Y. Lu, *J. Mater. Res.* **2017**, *32*, 2839.
[30] R. Xu, J. Yang, Y. Zhu, H. Yan, J. Pei, Y. W. Myint, S. Zhang, Y. Lu, *Nanoscale* **2016**, *8*, 129.
[31] T. Vogl, R. Lecamwasam, B. C. Buchler, Y. Lu, P. K. Lam, *ACS Photonics* **2019**, *6*, 1955.
[32] T. Vogl, M. W. Doherty, B. C. Buchler, Y. Lu, P. K. Lam, *Nanoscale* **2019**, *11*, 14362.
[33] T. Vogl, G. Campbell, B. C. Buchler, Y. Lu, P. K. Lam, *ACS Photonics* **2018**, *5*, 2305.
[34] T. Vogl, Y. Lu, P. Koy Lam, *J. Phys. D: Appl. Phys.* **2017**, *50*, 295101.
[35] T. Ahmed, S. Kuriakose, S. Abbas, M. J. S. Spencer, M. A. Rahman, M. Tahir, Y. Lu, P. Sonar, V. Bansal, M. Bhaskaran, S. Sriram, S. Walia, *Adv. Funct. Mater.* **2019**, *29*, 1.
[36] J. Lu, J. Yang, A. Carvalho, H. Liu, Y. Lu, C. H. Sow, *Acc. Chem. Res.* **2016**, *49*, 1806.
[37] L. Zhang, A. Sharma, Y. Zhu, Y. Zhang, B. Wang, M. Dong, H. T. Nguyen, Z. Wang, B. Wen, Y. Cao, B. Liu, X. Sun, J. Yang, Z. Li, A. Kar, Y. Shi, D. Macdonald, Z. Yu, X. Wang, Y. Lu, *Adv. Mater.* **2018**, *30*, 1803986.
[38] M. Tebyetekerwa, J. Zhang, K. Liang, T. Duong, G. P. Neupane, L. Zhang, B. Liu, T. N. Truong, R. Basnet, X. Qiao, Z. Yin, Y. Lu, D. Macdonald, H. T. Nguyen, *Adv. Mater.* **2019**, *31*, 1900522.
[39] L. Zhang, H. Yan, X. Sun, M. Dong, T. Yildirim, B. Wang, B. Wen, G. P. Neupane, A. Sharma, Y. Zhu, J. Zhang, K. Liang, B. Liu, H. T. Nguyen, D. Macdonald, Y. Lu, *Nanoscale* **2019**, *11*, 418.
[40] Y. Liu, B. N. Shivananju, Y. Wang, Y. Zhang, W. Yu, S. Xiao, T. Sun, W. Ma, H. Mu, S. Lin, H. Zhang, Y. Lu, C. W. Qiu, S. Li, Q. Bao, *ACS Appl. Mater. Interfaces* **2017**, *9*, 36137.
[41] J. Yang, Z. Wang, F. Wang, R. Xu, J. Tao, S. Zhang, Q. Qin, B. Luther-Davies, C. Jagadish, Z. Yu, Y. Lu, *Light: Sci. Appl.* **2016**, *5*, e16046.
[42] A. Castellanos-Gomez, M. Buscema, R. Molenaar, V. Singh, L. Janssen, H. S. J. Van Der Zant, G. A. Steele, *2D Mater.* **2014**, *1*, 011002.
[43] J. Pei, J. Yang, R. Xu, Y. H. Zeng, Y. W. Myint, S. Zhang, J. C. Zheng, Q. Qin, X. Wang, W. Jiang, Y. Lu, *Small* **2015**, *11*, 6384.
[44] T. Vogl, K. Sripathy, A. Sharma, P. Reddy, J. Sullivan, J. R. Machacek, L. Zhang, F. Karouta, B. C. Buchler, M. W. Doherty, Y. Lu, P. K. Lam, *Nat. Commun.* **2019**, *10*, 1202.
[45] Y. Zhu, Z. Li, L. Zhang, B. Wang, Z. Luo, J. Long, J. Yang, L. Fu, Y. Lu, *ACS Appl. Mater. Interfaces* **2018**, *10*, 43291.
[46] Y. Zhang, Y. Zhang, Q. Ji, J. Ju, H. Yuan, J. Shi, T. Gao, D. Ma, M. Liu, Y. Chen, X. Song, H. Y. Hwang, Y. Cui, Z. Liu, *ACS Nano* **2013**, *7*, 8963.
[47] S. Deng, V. Berry, *Mater. Today* **2016**, *19*, 197.
[48] J. Zang, S. Ryu, N. Pugno, Q. Wang, Q. Tu, M. J. Buehler, X. Zhao, *Nat. Mater.* **2013**, *12*, 321.
[49] T. Jiang, H. Liu, D. Huang, S. Zhang, Y. Li, X. Gong, Y. R. Shen, W. T. Liu, S. Wu, *Nat. Nanotechnol.* **2014**, *9*, 825.
[50] K. Liu, Q. Yan, M. Chen, W. Fan, Y. Sun, J. Suh, D. Fu, S. Lee, J. Zhou, S. Tongay, J. Ji, J. B. Neaton, J. Wu, *Nano Lett.* **2014**, *14*, 5097.
[51] W. Melitz, J. Shen, A. C. Kummel, S. Lee, *Surf. Sci. Rep.* **2011**, *66*, 1.
[52] M. Nonnenmacher, M. P. O'Boyle, H. K. Wickramasinghe, *Appl. Phys. Lett.* **1991**, *58*, 2921.
[53] S. Choi, Z. Shaolin, W. Yang, *J. Korean Phys. Soc.* **2014**, *64*, 1550.
[54] V. Kaushik, D. Varandani, B. R. Mehta, *J. Phys. Chem. C* **2015**, *119*, 20136.
[55] N. J. Lee, J. W. Yoo, Y. J. Choi, C. J. Kang, D. Y. Jeon, D. C. Kim, S. Seo, H. J. Chung, *Appl. Phys. Lett.* **2009**, *95*, 222107.
[56] Y. Li, C. Y. Xu, L. Zhen, *Appl. Phys. Lett.* **2013**, *102*, 143110.
[57] A. Castellanos-Gomez, E. Cappelluti, R. Roldán, N. Agraït, F. Guinea, G. Rubio-Bollinger, *Adv. Mater.* **2013**, *25*, 899.
[58] M. Rudan, *Physics of Semiconductor Devices* **2015**, Springer, Berlin.
[59] H. K. Henisch, *Proc. IEEE* **2008**, *74*, 894.
[60] J. Choi, H. Zhang, J. H. Choi, *ACS Nano* **2016**, *10*, 1671.
[61] H. M. Hill, A. F. Rigosi, K. T. Rim, G. W. Flynn, T. F. Heinz, *Nano Lett.* **2016**, *16*, 4831.
[62] K. Nowakowski, R. Van Bremen, H. J. W. Zandvliet, P. Bampoulis, *Nanoscale* **2019**, *11*, 5548.
[63] B. Amin, T. P. Kaloni, U. Schwingenschlögl, *RSC Adv.* **2014**, *4*, 34561.
[64] C. Ruppert, O. B. Aslan, T. F. Heinz, *Nano Lett.* **2014**, *14*, 6231.
[65] Z. Y. Zhao, Q. L. Liu, *Catal. Sci. Technol.* **2018**, *8*, 1867.
[66] J. Kwon, J. Y. Lee, Y. J. Yu, C. H. Lee, X. Cui, J. Hone, G. H. Lee, *Nanoscale* **2017**, *9*, 6151.
[67] T. Jiang, H. Liu, D. Huang, S. Zhang, Y. Li, X. Gong, Y. R. Shen, W. T. Liu, S. Wu, *Nat. Nanotechnol.* **2014**, *9*, 825.
[68] H. Mai, T. Lu, Q. Li, Z. Liu, Y. Li, F. Kremer, L. Li, R. L. Withers, H. Wen, Y. Liu, *ACS Appl. Mater. Interfaces* **2018**, *10*, 12781.